Characteristics and Thermal Shock Resistance of HVOF-Sprayed TiAlNb Coatings

Lei Wang[1] · Laiqi Zhang[1] · Qian Huang[1] · Changlei Zhang[1] · Lichun Zhang[2]

Abstract Two Ti-63.39Al-8.26Nb-0.2Y powders (powder 1 and powder 2) were fabricated by rapid in situ reaction and arc melting, respectively, then deposited on 316L stainless-steel substrate by the high-velocity oxygen fuel (HVOF) process. The phase composition, microstructure, porosity, microhardness, and adhesive strength of the two kinds of coating (DC1 and DC2) were characterized. DC1 had lower porosity, higher microhardness, and higher adhesive strength than DC2, which can be attributed to the difference in particle size distribution and mean particle size; a narrow particle size distribution and suitable mean particle size favor the formation of a HVOF coating with denser and more uniform microstructure. The thermal shock behavior was investigated by heating and water quenching from 600 °C to room temperature. The results showed that the failure of both TiAlNb coatings occurred due to spallation of the top coat, but the thermal shock resistance of DC2 was better than that of DC1. Thermal stress concentration caused by thermal expansion mismatch between the top coat and substrate was recognized as the major reason for TiAlNb coating failure.

Keywords TiAlNb · adhesive strength · microhardness · porosity · thermal shock resistance

✉ Laiqi Zhang
zhanglq@ustb.edu.cn

1   State Key Laboratory for Advanced Metals and Materials, University of Science and Technology Beijing, Beijing 100083, People's Republic of China

2   Department of Materials Science and Engineering, Institute of Materials Science, University of Connecticut, Storrs, CT 06269-3136, USA

Introduction

Hot dipping galvanization is one of the best and most effective methods employed to protect steel materials from corrosion in atmospheric environments (Ref 1-4). However, serious corrosion of equipment (e.g., sink rolls, supporting bearings, stabilizer, and supporting roll arms) remains a major problem in continuous galvanizing lines (CGLs) (Ref 5). The degradation and frequent failure of these equipment components result in severe production downtime and high maintenance costs. HVOF-sprayed WC-Co coatings are usually applied to 316L stainless-steel components used in CGLs, but their lifetime in liquid zinc is too short (about 1-2 weeks in duration) (Ref 2, 6-9). Therefore, the key to solve this problem is to identify a material that offers excellent corrosion resistance.

Numerous materials, such as ceramics (Ref 8-11), alloys (Ref 12-14), intermetallics (Ref 15-19), and other composite materials, have been selected and studied to improve the corrosion resistance of CGL components in molten zinc. However, almost none of these can satisfy the rigorous working conditions on CGLs.

In previous study, we found that TiAlNb alloys exhibit excellent resistance to corrosion by molten zinc (Ref 20). The lifetime of TiAlNb alloys in molten zinc exceeded 140 days. However, they cannot be used as integral workpieces due to their brittleness and hard machinability at room temperature. The HVOF TiAlNb coatings in the previous study also showed good resistance to corrosion in molten zinc. Zeng et al. (Ref 21) studied the effects of HVOF technology and substrate roughness on TiAlNb coatings and identified the optimal process. Zeng (Ref 22) also verified the influence of different kinds of bond coat on the mechanical behavior of TiAlNb coatings, concluding that the most suitable and cost-efficient bond coat for

TiAlNb coating was NiCrAl. However, TiAlNb powders prepared by the arc melting and crushing method showed polyhedral shape and a broad particle size distribution. During the HVOF process, this polyhedral shape and broad particle size distribution of the TiAlNb powder resulted in inhomogeneous heating and acceleration, and increased the formation of defects (Ref 22). In addition, it takes time and effort to crush such powder to a size range suitable for HVOF spraying due to the compact structure of TiAlNb alloy.

In the present work, TiAlNb powders were prepared using a novel in situ reaction technique, in contrast to the fabrication of TiAlNb powders by the arc melting method. TiAlNb coatings were deposited on 316L stainless-steel substrate by a HVOF process. The microstructure, phase composition, porosity, microhardness, and adhesive strength of the TiAlNb coatings were characterized. The thermal shock performance of the TiAlNb coatings was tested by heating and water quenching, and the corresponding failure mechanism is discussed.

Experimental Procedures

Powder and Specimen Preparation

Ti-63.39Al-8.26Nb-0.2Y (at.%) alloy powders used as the top-coat material were fabricated by in situ reaction and arc melting, respectively, as follows:

1. Powder 1 was rapidly synthesized using a novel in situ reaction technique from titanium (99.5 wt.% purity, 38 μm), aluminum (99.5 wt.% purity, 45 μm), niobium (99.5 wt.% purity, 20 μm), and yttrium (99 wt.% purity, 38 μm) powders as raw materials. To ensure compositional uniformity, the raw powders were mixed in a ball miller (QM-QX4, Nanjing, China; CGr15 milling ball, 300 r/min) for 3 h in a stainless-steel pot with alcohol as medium. The ratio of the milling ball to material was 1:1. The mixed powders were synthesized by in situ reaction at 1200 °C for 1 h in a vacuum oven furnace after vacuum drying. After mechanical crushing using a shake crusher (GJ-1, Shanghai, China), powder 1 was obtained by sieving with a 325 mesh sifter.

2. Powder 2 was prepared by arc melting using a nonconsumable electrode under high-purity argon from high-purity titanium chip, aluminum, yttrium, and Nb-Al master alloy (Nb 74.48 wt.%, Al 25.52 wt.%). To ensure compositional uniformity, each button was melted for five times. Powder 2 was obtained by sieving with a 325 mesh sifter after mechanical crushing using a shake crusher.

Commercially available NiCrAl powder with nominal composition Ni-20Cr-5Al (wt.%) of 10-45 μm offered by Langqiao Material Technology Co., Ltd. was used as the bond coat material. Substrate samples were cut from commercial 316L stainless steel (Cr 18-20, Ni 10-14, Mo 2-3, Mn ≤ 2, Si ≤ 1, Fe balance, in wt.%).

Spraying Conditions

TiAlNb coatings, composed of a NiCrAl bond coat (150 μm in thickness) and a TiAlNb top coat (300 μm in thickness), were deposited by the HVOF process. The TiAlNb top coat of the double-layer coatings (labeled DC1 and DC2) was fabricated using powder 1 or powder 2, respectively. The HVOF process was carried out using JP-8000 HVOF equipment. Prior to deposition, the substrate was degreased then grit blasted with 40 mesh Al_2O_3 under air pressure of 0.4 MPa. The HVOF spraying parameters are presented in Table 1.

Characterization

Porosity was determined by image analysis on the cross-section of the samples. Optical image analysis was used to calculate the area percentage of open and connected pores to determine the porosity. The porosity value of each sample was obtained by averaging about ten measurements.

Vickers microhardness tests were conducted with 100 g load and 15 s dwell time using a microhardness tester. The microhardness distribution on the cross-section of each coating was measured at each distance from the substrate to the coating surface in the thickness direction. The microhardness values at each data point mentioned in the experimental results were obtained by averaging about ten measurements.

Tensile testing was carried out according to the ASTM standard method (ASTM-C633-01). In this test, two cylindrical rods (Φ25.4 mm × 50 mm), one with a coating on the surface and the other without, were bonded by

Table 1 Spraying parameters for TiAlNb coatings

Parameter	Unit	NiCrAl bond coat	TiAlNb top coat
Kerosene flux	GPH	4.5	4.5
Oxygen flux	GPH	1650	1650
Carrier gas flux	SCFH	22	20
Feed rate	g/min	60	60
Spray distance	mm	360	330
Barrel length	inch	4	4
Spray gun velocity	mm s^{-1}	450	450

commercially available adhesive resin (epoxy resin E-7, Shanghai Huayi Resin Co., Ltd., China) which had normal strength of 80 MPa. A schematic of the adhesive strength tensile test is shown in Fig. 1. The specimens were kept in an oven at 100 °C for a holding time of 3 h then finally cooled down to room temperature. The samples were connected by rods through threaded holes. The rods were fixed into the grips of a tensile test machine. The tensile adhesive strength was measured using a material tester (100-kN load cell, Shenzhen, China) at cross-head speed of 1 mm/min. The adhesive strength value for each sample was determined as the average of three measurements.

The coatings were subjected to thermal shock testing using the heating and water quenching method to evaluate their lifetime. The coatings were deposited onto 316L stainless substrate with dimensions of $\Phi 20$ mm $\times$ 5 mm. The samples were heated at 600 °C and held for 15 min in a muffle furnace, then quickly dropped into water and cooled down to room temperature. The samples were taken out, dried, and returned to the furnace to repeat the aforementioned process. The number of thermal cycles at which a visible crack or spallation occurred on the surface of the top coat was recorded. Spallation of more than 20% of the top coat was adopted as the criterion for coating failure (i.e., the thermal cycling lifetime of the coating). Five specimens were tested to obtain the average thermal shock lifetime of the coatings.

Laser apparatus for grain size distribution analysis (Malvern, Mastersizer 3000, UK) was applied to study the particle size distribution of the experimental powder. The phase composition of the powder and as-sprayed coating was identified by x-ray diffraction analysis (Rigaku, SmartLab, Japan) using Cu K$_\alpha$ radiation in the 2θ angle range of 10°-100°. The morphology of the powder and as-sprayed coating was observed by scanning electron microscopy (Zeiss, ZeissAuriga, German) coupled with energy-dispersive x-ray spectroscopy (EDS).
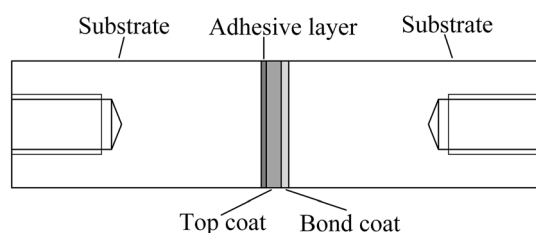

Fig. 1 Schematic of adhesive strength tensile test

Results and Discussion

Microstructure and Phase Composition

The morphology and particle size distribution of powder 1 and powder 2 are shown in Fig. 2. As shown in Fig. 2(a) and (b), the morphology of powder 1 and powder 2 used as top-coat materials showed irregular shape, which is expected to have an impact on the powder feeding during the HVOF process (Ref 23). From Fig. 2(c) and (d), it can be seen that the mean particle size of powder 1 (34.7 µm) was greater than that of powder 2 (20.1 µm). The particle size distribution (PSD) of powder 1 (1.25) was narrower than that of powder 2 (1.83). The suitable particle size distribution for JP-8000 HVOF equipment is from 15 to 45 µm. The narrow size distribution of powder 1 is beneficial for coating deposition by the HVOF process.

The XRD patterns of the powders and as-sprayed coatings are shown in Fig. 3(a) and (b), respectively. According to these XRD results, it can be concluded that both powder 1 and powder 2 consisted of γ (TiAl), and η [(Ti,Nb)Al$_3$] phases. In comparison with the XRD patterns of the powders, α$_2$ (Ti$_3$Al) phase appeared for the corresponding as-sprayed coatings. During the HVOF process, the powder experiences high temperatures and melts. After having been sprayed, the particles reached the 316L substrate and cooled down to room temperature rapidly. The high cooling rate induced formation of the metastable α$_2$ phase during the HVOF process (Ref 21, 22).

The surface morphology of DC1 and DC2 is shown in Fig. 4(a) and (b). The coating surface is relatively complete, and no macrocracks or spallation were observed. The high-magnification micrographs of DC1 and DC2 in Fig. 4(c) and (d) reveal that the coating surfaces showed complex features, composed of voids, microcracks, and molten particles. The surface morphology was determined by the extent of melting of the powder particles. Voids present in the surface of the coatings may be due to incomplete melting of particles. Some powder particles do not melt completely, because the heating time is very short. Agglomeration of partially melted particles and the high solidification speed are the main reasons for void formation (Ref 24). The microcracks may be generated due to the tensile stress when the molten droplets impact, spread, and are quenched to the substrate temperature or form deposited splats (Ref 25). Microcracks may also form due to the thermal stress attributed to the thermal expansion mismatch between the substrate and top coat during the HVOF process. These are all typical characteristics of coatings deposited by the HVOF process.

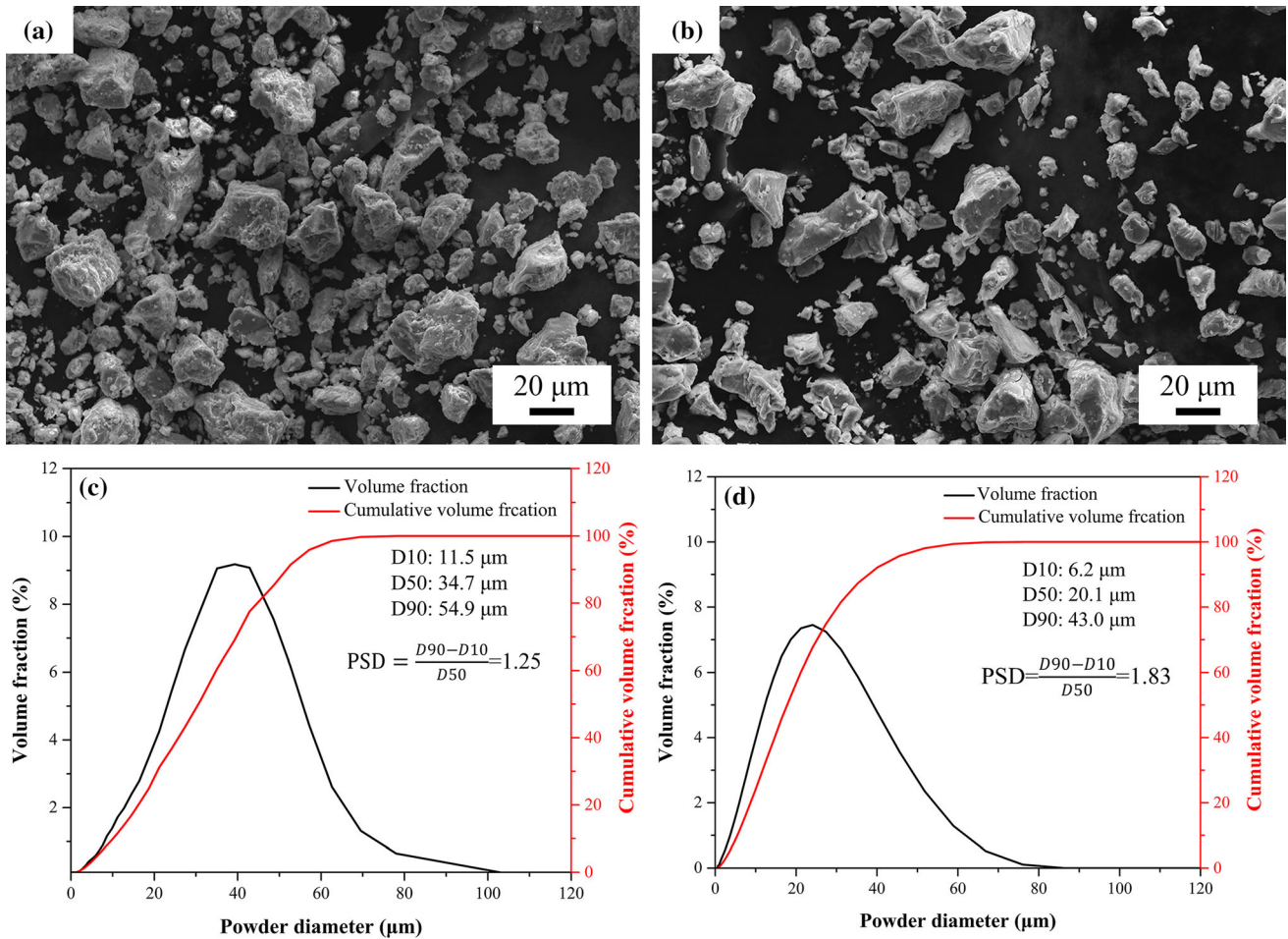Figure 5 shows the cross-sectional morphology of DC1 and DC2. As shown in Fig. 5(a) and (b), the TiAlNb

Fig. 2 Micrographs and particle size distribution of HVOF-sprayed powders: (a), (c) powder 1 and (b), (d) powder 2
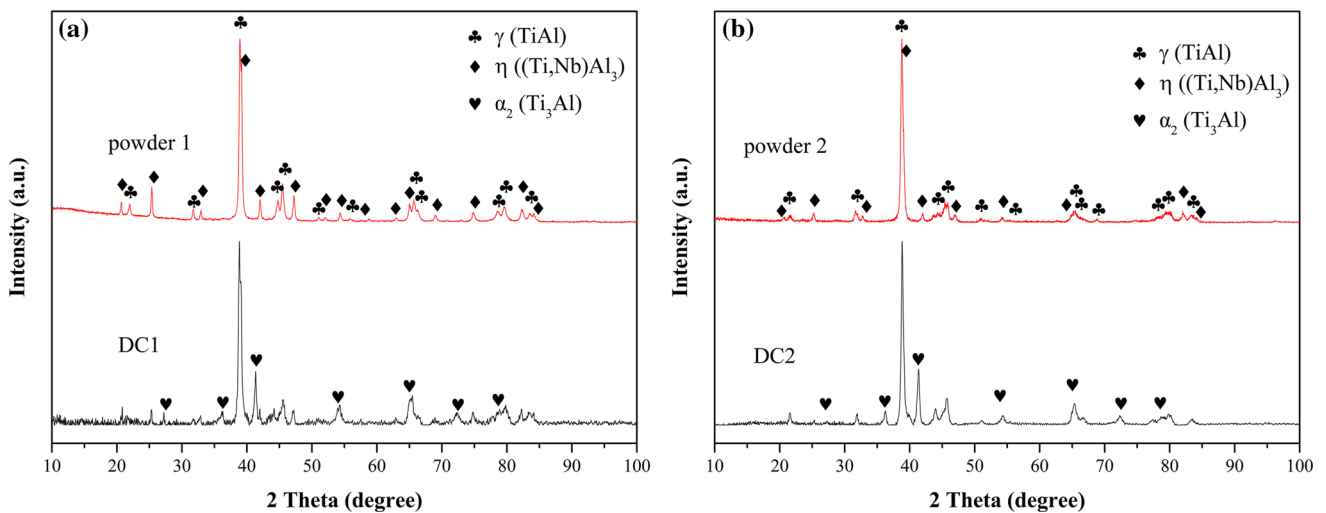

Fig. 3 XRD patterns of TiAlNb powders and corresponding as-sprayed coatings

coatings were composed of an NiCrAl bond coat and a TiAlNb top coat. The interfaces between the substrate and bond coat as well as between the bond coat and top coat were well bonded without obvious cracks. As seen from Fig. 5(c) and (d), DC1 and DC2 exhibited typical lamellar structure, which is also a typical feature of HVOF coatings.

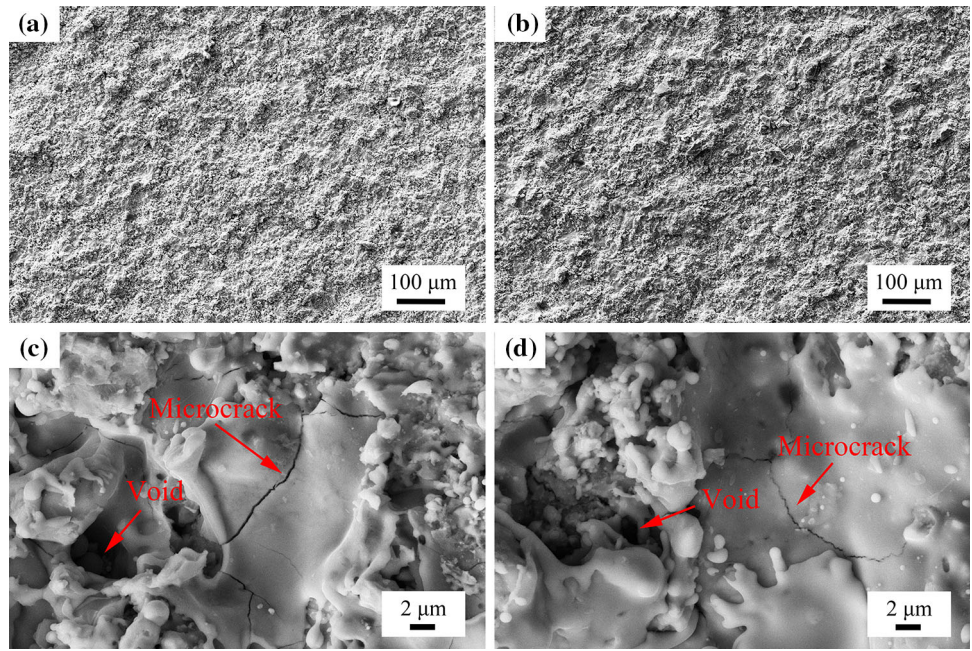**Fig. 4** Surface micrographs of (a) DC1 and (b) DC2, and (c) and (d) corresponding magnified portions

Fig. 5 Cross-sectional micrographs of (a) DC1 and (b) DC2, and (c) and (d) corresponding magnified portions
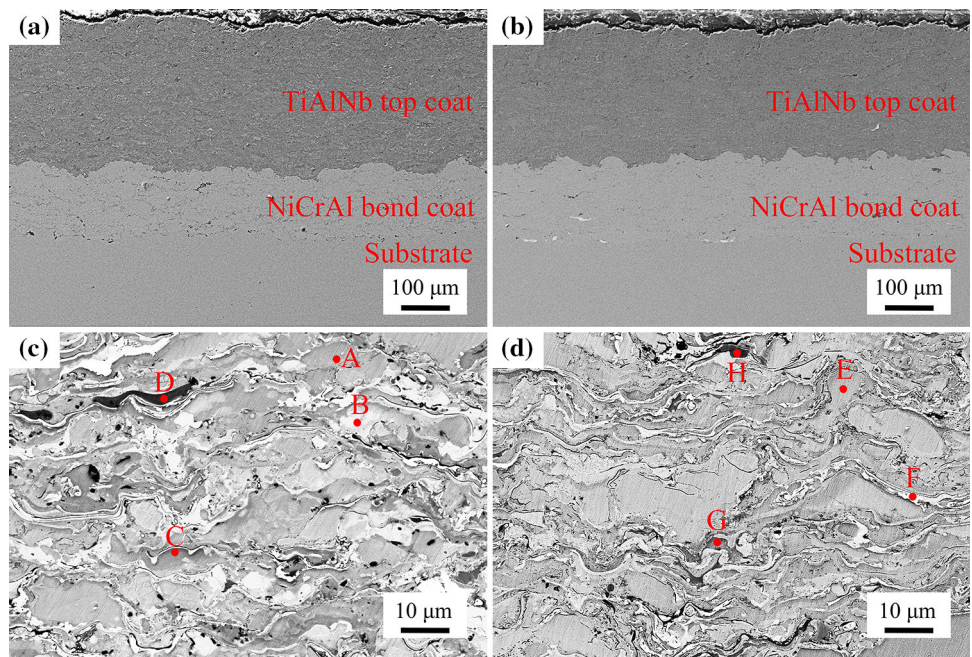

Table 2 Chemical composition (in at.%) results by EDS from Fig. 5(c)

Area	Ti	Al	Nb	Y	O	Phase
A	37.22	58.81	3.97	0	0	γ
B	10.53	71.89	14.75	0	2.83	η
C	62.94	27.96	5.00	0	4.10	α_2
D	9.42	22.55	2.52	0.45	65.06	Oxide

Table 3 Chemical composition (in at.%) results by EDS from Fig. 5(d)

Area	Ti	Al	Nb	Y	O	Phase
E	37.88	54.25	7.87	0	0	γ
F	10.19	74.12	12.70	0	2.99	η
G	63.43	24.82	8.54	0	3.21	α_2
H	7.87	25.56	3.20	0.33	63.04	Oxide

Table 2 and 3 present the chemical compositions of the corresponding areas in Fig. 5(c) and (d). Area A and E, B and F, and C and G correspond to γ, η, and α$_2$ phases, respectively. Areas D and H correspond to oxides.

Porosity and Microhardness

As shown in Fig. 6, the porosity of DC1 (0.86%) was lower than that of DC2 (1.18%). This is probably because the raw TiAlNb powder used for DC1 had a narrower size distribution than that used for DC2, as shown in Fig. 2. The particle size distribution of the powder was relatively narrow, which is important for its consistent melting in the flame (Ref 26). In the HVOF process, the narrower size distribution of the raw powder used in DC1 will lead to more homogeneous heating and acceleration and thus the formation of fewer defects and pores.

The results of the microhardness measurements are shown in Fig. 7, revealing the microhardness profiles across the cross-section of the coatings as a function of distance from the substrate to the top surface. Each data point in Fig. 7 is the mean of ten measurements, with a bar showing the standard deviation. The microhardness of the TiAlNb top coat was higher than that of the bond coat or substrate. Compared with DC2, the TiAlNb top coat of DC1 exhibited higher microhardness. The porosity, oxidization, and unmelted and semimelted particles in the coating have a significant effect on its microhardness according to literature (Ref 27, 28). Excessive porosity in the coating can cause a decrease in the microhardness. It is speculated that the decrease in the microhardness of DC2 is due to its high porosity.
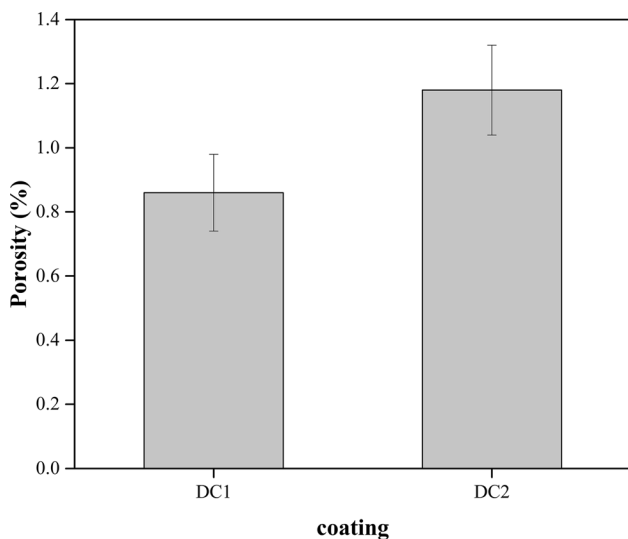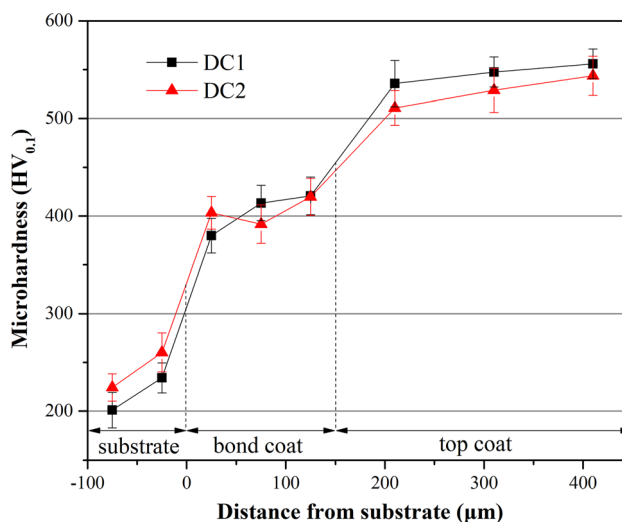

Fig. 6 Porosity of TiAlNb coatings (DC1 and DC2)

Fig. 7 Microhardness of TiAlNb coatings from substrate to coating surface

Adhesive Strength

The measured adhesive strength values of the TiAlNb coatings are presented in Table 4, revealing that the average adhesive strength of DC1 (65.8 MPa) was about 50.9% higher than that of DC2 (43.6 MPa). Our previous work revealed an average adhesive strength of 46 MPa for a TiAlNb coating with a NiCrAl bond coat produced by the HVOF process (Ref 22). Therefore, the adhesive strengths measured for the TiAlNb coatings in this work are both feasible and desirable. This indicates that the spraying parameters selected for the HVOF process (Table 1) were correct.

After tensile testing, the surface failure of the coatings was examined. In general, after applying tensile stress exceeding the adhesive strength of the coatings, failure can initiate within the bond coat, within the top coat, or at the top coat/bond coat interface (also called cohesive failure). Meanwhile, the term "adhesive failure" denotes a failure occurring at the interface between the bond coat and substrate (Ref 29-32). Figure 8 shows two fracture surfaces and the corresponding EDS analysis after tensile tests, being representative of such distinctive failure behaviors. Elemental composition analysis in areas a and b marked in Fig. 8(a) and (b) revealed elements from both the top coat and bond coat. The failure of DC2 occurred at the top coat/bond coat interface, i.e., cohesive failure, indicating the weak cohesion strength of the TiAlNb coating. The failure of DC1 was a combination of both cohesive failure and adhesive failure.

The adhesive strength of a coating depends on many parameters; some of the important ones include the surface roughness and porosity of the coating (Ref 33, 34). Powder 2 had a much broader particle size distribution than powder
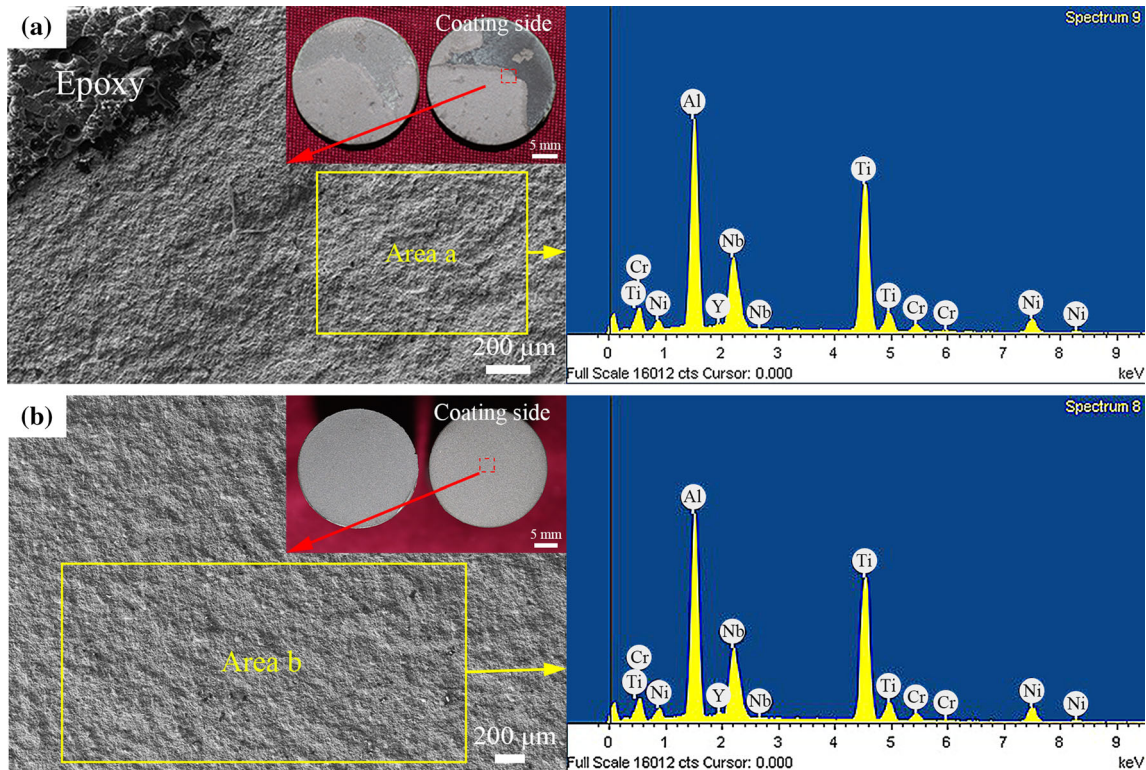
Fig. 8 Surface micrographs and EDS analysis of (a) DC1 and (b) DC2 after tensile testing

1. When a powder with a broader size distribution is sprayed by the HVOF process, gaps or pores tend to form between adjacent particles or between the top coat and bond coat. The presence of such high porosity is not conducive to the improvement of the adhesive strength.

Thermal Shock Behavior and Failure Analysis

The thermal shock lifetime of DC1 and DC2 at temperature of 600 °C is shown in Fig. 9. It was seen that the initial spallation of DC1 started to appear after 41 thermal shock cycles, extending to 20% of the TiAlNb top coat after 81 thermal shock cycles. Meanwhile, the number of cycles required for initial spallation and the thermal shock lifetime of DC2 were found to be 44 and 91, respectively. The thermal shock lifetime of DC2 was thus slightly longer than that of DC1. For comparison, the thermal shock lifetime of Al_2O_3-TiO_2 coating was reported to be about 100 cycles (Ref 11). This prolonged thermal shock lifetime of DC2 can be attributed to the relatively high porosity in the initial coating. The preexistence of porosity seemed to reduce the thermal mismatch stress and prolong the lifetime of the coating during thermal shock tests (Ref 35).

Figure 10 shows surface macrographs of DC1 and DC2 after different numbers of thermal cycles during the thermal shock tests. In comparison with the surface morphologies of the as-sprayed DC1 and DC2 (Fig. 10a and d),
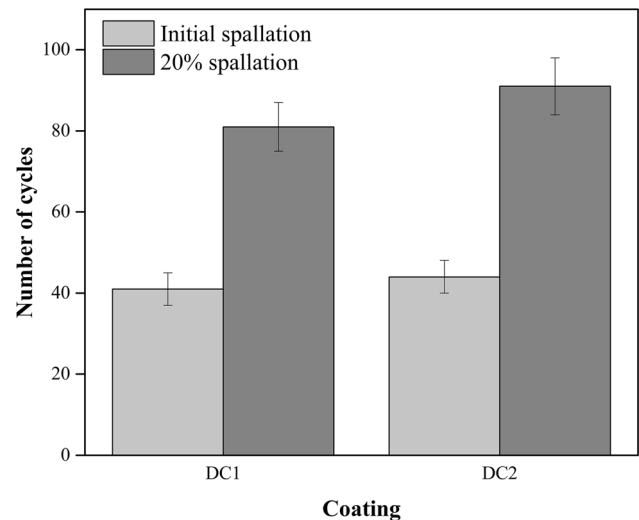

Fig. 9 Thermal shock lifetime of DC1 and DC2

Fig. 10(b) and (e) show that small-scale damage occurred initially at the extreme edges of the coatings after 41 and 44 cycles, respectively. The initial spallation originating at the edges of the coating samples is caused by stress concentration effects that occur there during the severe heating and cooling conditions. Relatively higher stress concentration is usually generated at edges when compared with the central region of the sample. Other studies (Ref 35-38)

have also mentioned the effect of edges on failure during thermal shock testing. This small-scale spallation is expected to propagate to adjacent areas during thermal shock cycling, eventually leading to failure of the coatings (Fig. 10c and f) after 81 and 91 cycles, respectively. This is a typical failure mechanism during thermal shock testing of HVOF coatings. In addition, the surface of the TiAlNb coatings showed a variation in color, with white spots being observed. These spots emerge due to impurities derived from the quenching water (Ref 39).

Figure 11 shows cross-sectional micrographs of DC1 and DC2 after thermal shock testing. In general, two kinds of typical cracks are formed in TiAlNb coatings after thermal cycling. As shown in Fig. 11(a) and (c), vertical cracks perpendicular to the thickness direction of the coatings can be clearly seen in the surface of the TiAlNb top coat of DC1 and DC2, whereas horizontal cracks can be seen at the interface between the TiAlNb top coat and NiCrAl bond coat in Fig. 11(b) and (d), respectively.

Figure 12 shows the failure mechanism of the TiAlNb coating during thermal shock cycling. The volume change and the stress states in different regions vary during the heating and cooling cycles due to the thermal expansion coefficient mismatch between the top coat (13.01×10^{-6} K^{-1}) and bond coat (13.62×10^{-6} K^{-1}) or bond coat and substrate (17.9×10^{-6} K^{-1}) (Ref 22). In the heating stage, the surface of the top coat undergoes tensile stress, as shown in Fig. 12(a). Meanwhile, in the cooling stage, the surface of the top coat suffers compressive stress, as shown in Fig. 12(b). As the thermal shock cycles continue, the coating surface will accumulate residual tensile stress, which will induce a bending effect (Fig. 12c). The surface of the top coat and the interface between the top coat and bond coat will generate a stress concentration due to this bending effect, as shown in Fig. 12(d). Vertical cracks initiate at the surface of the top coat when this residual tensile stress exceeds the fracture strength of the TiAlNb material. In addition, pre-existing surface microcracks (Fig. 4c and d) may also be a source of vertical cracks. They can then propagate perpendicular to the thickness direction during thermal shock cycling, which can be ascribed to the brittleness of the TiAlNb material. Structural defects such as pores and intersplat cracks are the main sources of crack formation in the TiAlNb top coat. Meanwhile, as the thermal shock cycles continue, horizontal cracks occur at the weakest bonding locations and will propagate at the interface between the top coat and bond coat owing to the thermal stress concentration. The development and coalescence of surface vertical cracks and interface horizontal cracks will eventually result in the failure of the TiAlNb coating (Fig. 12e). As a result, cracks are easily generated and will propagate during the thermal shock test, eventually causing coating failure. It has been reported that zinc atoms can diffuse into the coating via vertical cracks generated by thermal shocks, react with the substrate, and in turn accelerate the propagation of cracks. This will eventually lead to coating failure (Ref 8). In addition, the horizontal cracks will also extend and connect to the vertical cracks. The top coat may thus be segmented into independent parts, which will eventually fall off (Ref 25). It should be emphasized here that it is relatively
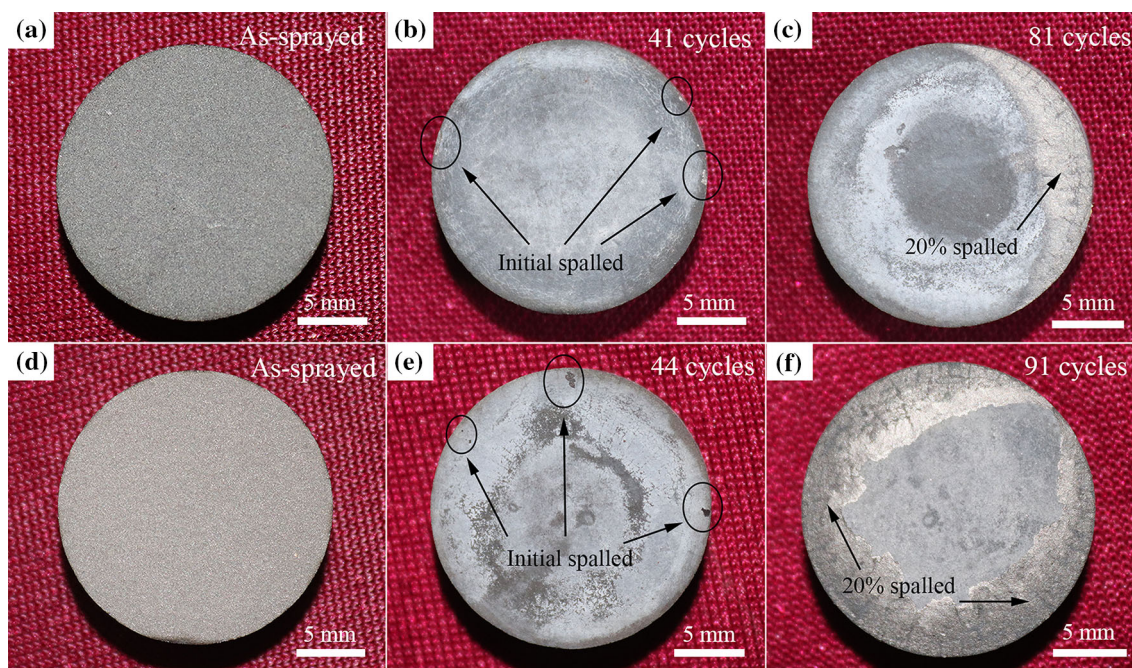

Fig. 10 Typical macrographs of (a-c) DC1 and (d-f) DC2 during thermal shock tests

Fig. 11 Cross-sectional micrographs of (a), (b) DC1 and (c), (d) DC2 after thermal shock tests
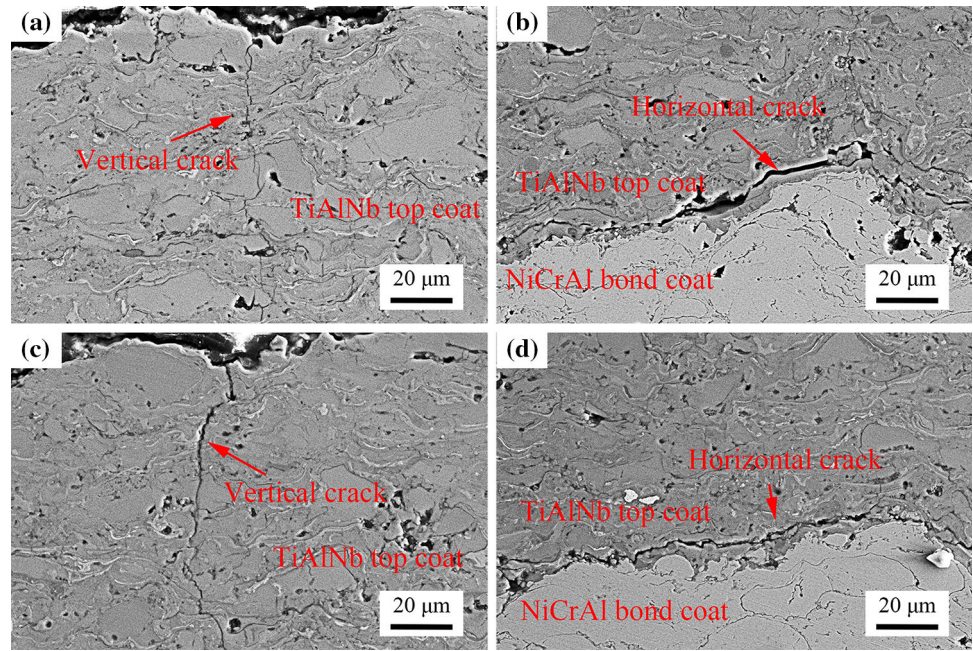

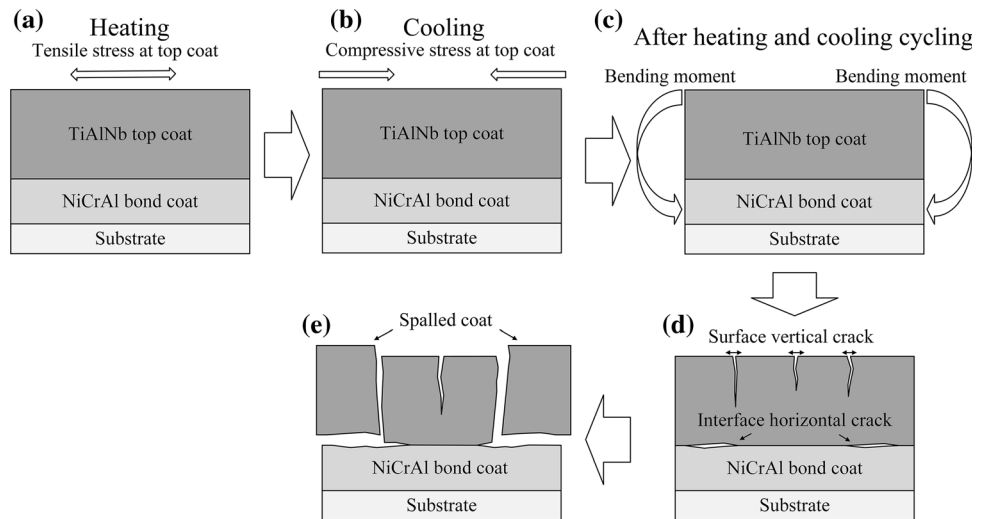**Fig. 12** Schematic illustration of failure of TiAlNb coating after thermal shock cycling

Table 4 Adhesive strength of TiAlNb coatings

Coating type	Bonding strength, MPa				Type of failure
	Sample 1	Sample 2	Sample 3	Average	
DC1	65.2	67.6	64.5	65.8	Cohesive failure and adhesive failure
DC2	42.7	47.8	40.2	43.6	Cohesive failure

important to suppress such generation and propagation of different types of cracks to improve the thermal shock resistance of such coatings.

Conclusions

Two kinds of Ti-63.39Al-8.26Nb-0.2Y alloy powder (named powder 1 and powder 2) were fabricated by in situ reaction and arc melting, respectively. DC1 and DC2 were deposited on 316L substrate using raw powder 1 and

powder 2 by a HVOF process, respectively. The phase composition, microstructure, porosity, microhardness, adhesive strength, and thermal shock behavior of these two TiAlNb coatings were investigated and compared. The following conclusions can be drawn:

1. Compared with the raw TiAlNb feedstock powders, a new α_2 phase appeared in DC1 and DC2. DC1 showed lower porosity, higher microhardness, and higher adhesive strength than DC2. Overall, a narrower particle size distribution and suitable mean particle size favor the formation of HVOF coatings with denser and uniform microstructure. The in situ reaction method could be considered as a suitable powder manufacturing method for CGL applications.

2. The thermal shock resistance of DC2 was slightly higher than that of DC1. The prolonged thermal shock lifetime of DC2 can be attributed to its relatively high porosity.

3. During thermal shock testing, both DC1 and DC2 failed due to spallation of the top coat. Thermal stress due to the thermal expansion coefficient mismatch between the top coat and substrate is the major reason for this failure during thermal shock testing of the TiAlNb coatings. Stress concentration leads to the formation and growth of cracks, and the development and coalescence of vertical and horizontal cracks eventually resulted in failure of the TiAlNb coatings.

References

1. S. Ma, J. Xing, P. Lyu, Y. Wang, and G. Liu, Multiphase Interface Structure Induced Erosion Resistance of Directional Solidified Fe-B Alloy in Flow Liquid Zinc, *Mater. Lett.*, 2018, **211**, p 281-284

2. N. Setargew, W.Y. Danielyuen, and J.C. Hodges, Intermetallic Spike Growth Mechanisms in 316L Stainless Steel in Contact with Molten 55%Al-Zn Metal Coating Alloy, *Metall. Res. Technol.*, 2016, **113**(4), p 409

3. X. Fang, Y. Wang, Y. Zhang, S. Feng, J. Du, D. Liu, T. Ouyang, J. Suo, and S. Cai, Improving the Corrosion Resistance of Fe-21Cr-9Mn Alloy in Liquid Zinc by Heat Treatment, *Corros. Sci.*, 2016, **111**, p 362-369

4. S. Ma, J. Xing, D. Yi, H. Fu, G. Liu, and S. Ma, Microstructure and Corrosion Behavior of Cast Fe-B Alloys Dipped into Liquid Zinc Bath, *Mater. Charact.*, 2010, **61**(9), p 866-872

5. X. Ren, X. Mei, J. She, and J. Ma, Materials Resistance to Liquid Zinc Corrosion on Surface of Sink Roll, *J. Iron Steel Res. Int.*, 2007, **14**(5), p 130-136

6. J. Xu, M.A. Bright, X. Liu, and E. Barbero, Liquid Metal Corrosion of 316L Stainless Steel, 410 Stainless Steel, and 1015

7. Carbon Steel in a Molten Zinc Bath, *Metall. Mater. Trans. A*, 2007, **38**(11), p 2727-2736

7. X. Liu, E. Barbero, J. Xu, M. Burris, K. Chang, and V. Sikka, Liquid Metal Corrosion of 316L, Fe₃Al, and FeCrSi in Molten Zn-Al Baths, *Metall. Mater. Trans. A*, 2005, **36**(8), p 2049-2058

8. J. Zhang, C. Deng, J. Song, C. Deng, M. Liu, and K. Zhou, MoB-CoCr as Alternatives to WC-12Co for Stainless Steel Protective Coating and Its Corrosion Behavior in Molten Zinc, *Surf. Coat. Technol.*, 2013, **235**, p 811-818

9. B.G. Seong, S.Y. Hwang, M.C. Kim, and K.Y. Kim, Reaction of WC-Co Coating with Molten Zinc in a Zinc Pot of a Continuous Galvanizing Line, *Surf. Coat. Technol.*, 2001, **138**(1), p 101-110

10. Y. Dong, D. Yan, J. He, J. Zhang, and X. Li, Degradation Behaviour of ZrO₂-Ni/Al Gradient Coatings in Molten Zn, *Surf. Coat. Technol.*, 2006, **201**(6), p 2455-2459

11. S.H. Yao, Y.L. Su, H.Y. Shu, C.I. Lee, and Z.L. You, Comparative Study on Nano-Structural and Traditional Al₂O₃-13TiO₂ Air Plasma Sprayed Coatings and their Thermal Shock Performance, *Key Eng. Mater.*, 2017, **739**, p 103-107

12. G. Zhang, D. Li, N. Zhang, N. Zhang, and S. Duan, Thermal-Sprayed Coatings on Bushing and Sleeve-Pipe Surfaces in Continuous Galvanizing Sinking Roller Production Line Applications, *Coatings*, 2017, **7**(8), p 113

13. R.T. Loto and E. Özcan, Corrosion Resistance Studies of Austenitic Stainless Steel Grades in Molten Zinc-Aluminum Alloy Galvanizing Bath, *J. Fail. Anal. Prev.*, 2016, **16**(3), p 427-437

14. Y. Liu, M. Tang, Y. Song, C. Wu, H. Peng, X. Su, and J. Wang, Reactions of FeCr Alloys with Liquid Zinc in Hot-Dip Galvanizing, *Surf. Coat. Technol.*, 2015, **276**, p 714-720

15. D. Yan, J. He, B. Tian, Y. Dong, X. Li, J. Zhang, L. Xiao, and W. Jing, The Corrosion Behavior of Plasma Sprayed Fe₂Al₅ Coating in Molten Zn, *Surf. Coat. Technol.*, 2006, **201**(6), p 2662-2666

16. D. Yan, Y. Yang, Y. Dong, X. Chen, L. Wang, J. Zhang, and J. He, Phase Transitions of Plasma Sprayed Fe-Al Intermetallic Coating During Corrosion in Molten Zinc at 640 °C, *Intermetallics*, 2012, **22**, p 160-165

17. R.N. Ma, A. Du, Y.Z. Fan, S.J. Li, and X.M. Cao, Corrosion Behaviour of Stoichiometric Fe₃Si Alloy in Liquid Zinc, *Corros. Eng. Sci. Technol.*, 2014, **49**(3), p 236-240

18. W. Wang, J. Lin, Y. Wang, and G. Chen, Isothermal Corrosion Fe₃Si Alloy in Liquid Zinc, *J. Univ. Technol. B.*, 2007, **14**(1), p 52-55

19. J. Wang, H. Tu, B. Peng, X. Wang, F. Yin, and X. Su, The Effects of Zinc Bath Temperature on the Coating Growth Behavior of Reactive Steel, *Mater. Charact.*, 2009, **60**(11), p 1276-1279

20. J.P. Lin, W.J. Wang, Y.L. Wang, Z. Lin, and G.L. Chen, China patent CHN10011237.5 (2006)

21. H.J. Zeng, L.Q. Zhang, J.P. Lin, S.J. Zhang, and G.L. Chen, TiAlNb Intermetallic Compound Coating Prepared by High Velocity Oxy-Fuel Spraying, *Surf. Coat. Technol.*, 2011, **206**(1), p 178-184

22. H.J. Zeng, L.Q. Zhang, J.P. Lin, X.Y. He, Y.C. Zhang, and P. Jia, Influence of Bond Coats on the Microstructure and Mechanical Behaviors of HVOF-Deposited TiAlNb Coatings, *J. Therm. Spray Technol.*, 2012, **21**(6), p 1245-1256

23. Q. Wang, Z. Chen, L. Li, and G. Yang, The Parameters Optimization and Abrasion Wear Mechanism of Liquid Fuel HVOF Sprayed Bimodal WC-12Co Coating, *Surf. Coat. Technol.*, 2012, **206**(8-9), p 2233-2241

24. S. Chen, J. Xiang, J. Huang, and X. Zhao, Microstructures and Properties of Double-Ceramic-Layer Thermal Barrier Coatings of La₂(Zr₀.₇Ce₀.₃)₂O₇/8YSZ Made by Atmospheric Plasma Spraying, *Appl. Surf. Sci.*, 2015, **340**, p 173-181

25. M. Zhai, D. Li, Y. Zhao, X. Zhong, F. Shao, H. Zhao, C. Liu, and S. Tao, Comparative Study on Thermal Shock Behavior of Thick Thermal Barrier Coatings Fabricated with Nano-based YSZ

Suspension and Agglomerated Particles, *Ceram. Int.*, 2016, **42**(10), p 12172-12179

26. X. Zhong, H. Zhao, C. Liu, L. Wang, F. Shao, X. Zhou, S. Tao, and C. Ding, Improvement in Thermal Shock Resistance of Gadolinium Zirconate Coating by Addition of Nanostructured Yttria Partially-Stabilized Zirconia, *Ceram. Int.*, 2015, **41**(6), p 7318-7324

27. B.S. Sidhu, D. Puri, and S. Prakash, Mechanical and Metallurgical Properties of Plasma Sprayed and Laser Remelted Ni-20Cr and Stellite-6 Coatings, *J. Mater. Process. Technol.*, 2015, **159**(3), p 347-355

28. H.S. Sidhu, B.S. Sidhu, and S. Prakash, Mechanical and Microstructural Properties of HVOF Sprayed WC-Co and Cr_3C_2-NiCr Coatings on the Boiler Tube Steels Using LPG as the Fuel Gas, *J. Mater. Process. Technol.*, 2006, **171**(1), p 77-82

29. C.R.C. Lima and J.M. Guilemany, Adhesion Improvements of Thermal Barrier Coatings with HVOF Thermally Sprayed Bond Coats, *Surf. Coat. Technol.*, 2007, **201**(8), p 4694-4701

30. A.C. Karaoglanli, H. Dikici, and Y. Kucuk, Effects of Heat Treatment on Adhesion Strength of Thermal Barrier Coating Systems, *Eng. Fail. Anal.*, 2013, **32**, p 16-22

31. A.M. Khoddami, A. Sabour, and S.M.M. Hadavi, Microstructure Formation in Thermally-Sprayed Duplex and Functionally Graded NiCrAlY/Yttria-Stabilized Zirconia Coatings, *Surf. Coat. Technol.*, 2007, **201**(12), p 6019-6024

32. S. Dong, B. Song, G. Zhou, B. Hansz, H. Liao, and C. Coddet, Multi-layered Thermal Barrier Coatings Fabricated by Plasma-Spraying and Dry-Ice Blasting: Microstructure Characterization and Prolonged Lifetime, *Surf. Coat. Technol.*, 2013, **236**, p 557-567

33. S.R. Dhineshkumar, M. Duraiselvam, S. Natarajan, S.S. Panwar, T. Jana, and M.A. Khan, Enhanced Ablation Resistance Through Laser Glazing of Plasma Sprayed $LaTi_2Al_9O_{19}$-Based Functionally Graded Thermal Barrier Coating, *Ceram. Int.*, 2016, **42**(8), p 10184-10190

34. A. Vencl, S. Arostegui, G. Favaro, F. Zivic, M. Mrdak, S. Mitrović, and V. Popovic, Evaluation of Adhesion/Cohesion Bond Strength of the Thick Plasma Spray Coatings by Scratch Testing on Coatings Cross-Sections, *Tribol. Int.*, 2011, **44**(11), p 1281-1288

35. C. Giolli, A. Scrivani, G. Rizzi, F. Borgioli, G. Bolelli, and L. Lusvarghi, Failure Mechanism for Thermal Fatigue of Thermal Barrier Coating Systems, *J. Therm. Spray Technol.*, 2009, **18**(2), p 223-230

36. J. Wu, H. Guo, L. Zhou, L. Wang, and S. Gong, Microstructure and Thermal Properties of Plasma Sprayed Thermal Barrier Coatings from Nanostructured YSZ, *J. Therm. Spray Technol.*, 2010, **19**(6), p 1186-1194

37. H. Guo, Y. Wang, L. Wang, and S. Gong, Thermo-Physical Properties and Thermal Shock Resistance of Segmented $La_2Ce_2O_7$/YSZ Thermal Barrier Coatings, *J. Therm. Spray Technol.*, 2009, **18**(4), p 665-671

38. R. Ahmadi-Pidani, R. Shoja-Razavi, R. Mozafarinia, and H. Jamali, Improving the Thermal Shock Resistance of Plasma Sprayed CYSZ Thermal Barrier Coatings by Laser Surface Modification, *Opt. Laser. Eng.*, 2012, **50**(5), p 780-786

39. Y. Cao, Q. Wang, Y. Liu, X. Ning, and H. Wang, Characteristics and Thermal Cycling Behavior of Plasma-Sprayed $Ba(Mg_{1/3}Ta_{2/3})O_3$ Thermal Barrier Coatings, *Ceram. Int.*, 2017, **43**(14), p 10955-10959